Development of Interdigitated Capacitive Sensor for Real-Time Monitoring of Sub-Micron and Nanoscale Particulate Matters in Personal Sampling Device for Mining Environment

Doosan Back, Daniel Theisen, Weeseong Seo, *Member, IEEE*, Candace Su-Jung Tsai, and David B. Janes, *Member, IEEE*

***Abstract*—While current personal monitoring devices for mining industry are optimized for monitoring microscale particles, a higher resolution technique is required to detect sub-micron and nanoscale particulate matters (PM) due to smaller volume and mass of the particles. In this work, an interdigitated capacitive sensor is designed for monitoring sub-micron and nanoscale particle concentration in real-time for mining environment and other applicable environments. The 2 mm × 12 mm disposable sensor chip fits generic air sampling cassette housing. The re-usable readout board uses resistance-capacitance (RC) delay time constant for monitoring capacitance shift and data is recorded in real-time. The sensor showed clear response with respect to a commonly used test dust, and positive capacitance shift is observed after test. Among the collected particles, about 77 % are sub-micron and most of microparticles are agglomerates of sub-micron particles. A simulation study showed that our sensor response is in a region that is proportional to the particle volume collected on sensor. A comparison with gravimetric method showed that less than 1/1000 of collected particle mass on the sampler is responsible for sensor response due to radial distribution of particle deposition and sensor location. The sensor response is converted into a standard airborne mass particle concentration (g/m^3) to demonstrate a continuous monitoring of particle concentration. An incorporated microheater improved stable capacitive sensor reading under air flow and various humidity.**

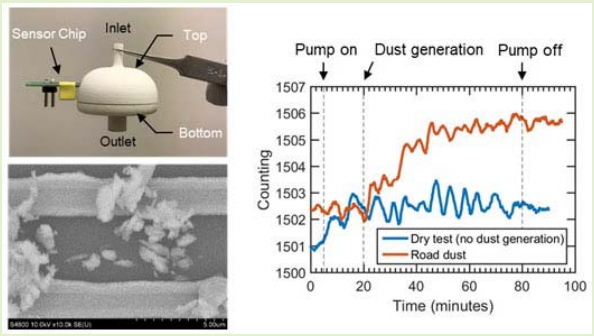

***Index Terms*—Particulate matter, capacitive sensor, nanoparticles, real-time monitoring, microheater.**

I. Introduction

PARTICULATE matter (PM) is a mixture of particles and droplets in air consisting of various compounds. PM exists everywhere in various sizes and some of the particles are toxic and respirable to human. Some work environments have more dangerous respirable particles than others and can cause harmful effects to human through inhalation. Miners in the mining environment are often exposed to higher level of hazardous particles such as coal, silica (SiO_2) and diesel exhaust. Continuous exposure to such particles can cause severe damage to the human respiratory system. For instance, exposure to mine dust can cause coal workers' pneumoconiosis (CWP), also known as black lung disease, which is very common in coal miners; it is reported that about 4,800 people in U.S. died because of CWP from 2005 to 2014 [1]. Workers mining minerals are at high risk for silicosis as they are exposed to mine dust containing high amount of silica. Accordingly, the National Institute for Occupational Safety and Health (NIOSH) recommends that workers' exposure to respirable coal mine dust should be limited to 1 mg/m^3 and crystalline silica should be limited to 0.05 mg/m^3 (up to 10 hours per day over a 40-hour work week) [2]. Recently, Mine Safety and Health Administration (MSHA) lowered the concentration limit of respirable coal mine dust from 1 mg/m^3 to 0.5 mg/m^3 for underground and surface coal mines [3].

Manuscript received April 10, 2020; accepted May 16, 2020. Date of publication May 20, 2020; date of current version September 3, 2020. This study was supported in part by the Alpha Foundation for the Improvement of Mine Safety and Health, Inc. (ALPHA FOUNDATION), under Grant AFC518, in part by the Alpha Foundation Technology Development and Exploratory Research Fund, and in part by the Centers for Disease Control and Prevention under Grant T42OH009229-11. The associate editor coordinating the review of this article and approving it for publication was Dr. Ferran Reverter. *(Corresponding authors: Candace Su-Jung Tsai; David B. Janes.)*

Doosan Back, Weeseong Seo, and David B. Janes are with the School of Electrical and Computer Engineering, Purdue University, West Lafayette, IN 47907 USA, and also with the Birck Nanotechnology Center, Purdue University, West Lafayette, IN 47907 USA (e-mail: dback@purdue.edu; seo36@purdue.edu; janes@purdue.edu).

Daniel Theisen and Candace Su-Jung Tsai are with the Department of Environmental and Radiological Health Sciences, College of Veterinary Medicine and Biomedical Sciences, Colorado State University, Fort Collins, CO 80523 USA (e-mail: danielrtheisen@gmail.com; candace.tsai@colostate.edu).

Digital Object Identifier 10.1109/JSEN.2020.2995960

Some devices have been commercially developed to monitor air quality or collect airborne particles in the mining environments. The two broad approaches are: i) gravimetric filter sampling for particle collection and ii) direct reading of particle mass concentration. The gravimetric sampling is one of the oldest and most popular methods, since it was first introduced in 1950s. Higgins and Dewell first designed a personal sampler consisting of cyclone, filter holder and a small pump and workers wore the apparatus during work hours [4]. The concentration of dust is calculated by the average mass gain over the sampling time. The filter is then analyzed via electron microscopy and x-ray diffraction spectroscopy (XPS) to examine the accurate concentration and components of the collected particles such as silica [5], [6]. However, it requires several hours to collect enough particles and the samples are sent out for accurate analysis of the particles. On the other hand, direct reading of particle concentrations has been developed with various monitoring techniques. In 1973, Gravati presented a light scattering method to measure size distribution of PM in real time. This method has been developed to monitor PM concentrations by translating the sampler's light scattering into the corresponding concentration [7], [8]. Personal DataRAM (pDR) is one of the commercial devices which use the light scattering method and it was often used in underground gassy mines for making rough relative measurements [9]. Personal dust monitor (PDM) is another type of real-time instrument that uses a tapered-element oscillation microbalance (TEOM) to monitor the coal-dust concentration in the mining environment. TEOM was first introduced by Wang *et al.* where a replaceable filter cartridge is mounted to the tip of the tapered element, which oscillates like a tuning fork during operation [10]. The oscillation frequency changes in real-time with respect to the mass collected on the filter and the integrated particle mass can be analyzed by gravimetric method after measurement. The TEOM-based PDM is now a mandatory instrument to monitor dust exposure for workers in underground coal mines [11].

The advancement of nanotechnology naturally brought attention to the hazard of nanomaterials and the necessity for higher resolution monitoring systems. This concern is now raised to work places handling nanomaterials as well as underground mines [12], [13]. According to Heyder *et al.*, particle deposition efficiency in the human respiratory track varies with particle diameter; while the highest efficiency ($\sim$90 %) is at particle diameter of 10 μm and reduces to 15 % with decreased diameter, the efficiency starts increasing again when the diameter is 0.2 μm. The efficiency reaches almost 80 % with particle diameter of $\sim$0.01 μm [14]. Moreover, such particles can penetrate deep into the lung or other organs by circulating through the body [15]. Recent research has demonstrated that nanoparticles (NPs) have stronger and unique adverse health effects compared to micrometer-sized particles of the same material [16]–[18]. There is a clear need for an accurate method to characterize NP exposure. However, due to the smaller volume of particles as well as their smaller mass, detecting sub-micron and nanoparticles using current methods is challenging since it requires orders of magnitude higher sensitivity compared to detecting microscale particles. In parallel, there is an effort to change the mass-based regulation to number of NPs for accurate evaluations. While a number of government agencies and private entities have established mass-based occupational exposure limits (OELs) for carbon nanotubes (CNTs), one type of nanomaterial, some agencies have started to rely on number of concentrations [19].

Commercially available PM sensors are not yet developed to detect ultra-fine particles from noisy environment. For instance, the use of pDR is inhibited in gassy underground mines as it is impacted by moisture in the mine air and calibration using gravimetric measurement is necessary [9]. Therefore, it is not recommended for environments where accuracy is the topmost concern. In addition, NIOSH reported in 2013 that TEOM technique is not suitable for monitoring nanomaterials in the mining environment [20]. Mine dust contains a portion of respirable particles in nanometer sizes as well as in microscale [21]. However, current devices are mainly affected by larger particles while the response from smaller particles are masked by the response of the larger particles.

Several studies have shown the possibilities of high-resolution particle detection sensors using advanced technologies such as microelectromechanical systems (MEMS). Sensors made with microfabricated cantilevers [22] or acoustic resonator [23], [24] allow the detection of airborne particles whose masses are from pico-gram (pg) to nano-gram (ng). Hajjam *et al.* designed a micromechanical acoustic resonator and detected individual particles of 1μm diameter (1-2 pg) using a table-top network analyzer [25]. Techniques using optical scattering has also developed to detect smaller particles. Commercial optical particle counters (OPC) have detection limit around 0.3 μm by analyzing the scattered light. Particles with tens of nanometers of diameter are difficult to detect due to the limitation of wavelength; Rayleigh scattering occurs when particle are much smaller than the wavelength of light (i.e. $\sim$1/10 of the wavelength). The state-of-the-art technology such as scanning mobility particle sizer (SMPS) detects such nanoparticles by enlarging them using condensation in a supersaturated gas, reaching a detection resolution of few nanometers [26]. However, SMPS cannot be used in the mining environment and it is not optimized for personal monitoring. Detection of single nanoparticle could be achieved without condensation by using optical microcavities [27] and nanofiber arrays [28]. In spite of the improved sensor sensitivity, there are limitations on the miniaturization of system; the optical scattering technique requires a laser source, multiple photodetectors, and a closed chamber to minimize environmental effect [29]. This may be overcome with advanced semiconductor technologies such as laser diodes, but nanoparticle detection with condensation needs additional equipment such as condenser and alcohol reservoir [30]. MEMS cantilevers and microcavities could be portable but it is still difficult to detect ultra-fine particles without laboratory equipment due to noise [31], [32]. There are a couple of recently available portable devices for measuring particles in the respirable or ultra-fine size ranges, unfortunately they are not applicable to the mining environment yet [33], [34].

Unlike the methods mentioned above, capacitive sensors detect particles by capacitance shift due to the dielectric properties of deposited particles. Evans and York first demonstrated a sensor chip for particle detection using interdigitated capacitive sensor [35]. The sensor chip includes a sensor array and readout circuit, and they showed 60 atto-farad (aF) of capacitance shift for a 50 μm particle deposited on the sensor. Ciccarella *et al.* demonstrated a capacitive sensor with low noise readout circuitry and measured 10 aF capacitance shift with a 5 μm diameter mineral talc particle [36]. Both works used custom-designed readout circuits to avoid the use of laboratory equipment and integrated with sensor in a single board. Due to electrical interface of capacitive sensor, it allows an easy integration with readout circuits. Therefore, it has more potential for miniaturization than other techniques such that the capacitive sensor can be integrated with generic air sampling cassette, or pocket-sized sensor and smartphone-embedded sensor can be made [37].

While the previous capacitance sensing approaches demonstrated microscale particle detection, sensor response for sub-micron and nanoscale regimes were not studied. In this work, we aimed to design and fabricate a capacitive sensor for sub-micrometer and nanoparticles in the respirable range. The proposed interdigitated capacitance sensor has detection capability of sub-micron and nanoscale particles in 1 mm $\times$ 1.5 mm sensing area. This miniaturized sensor enables an easy integration with standard sampling cassettes minimizing the interference of air flow for particle collection. The readout board utilizes resistance-capacitance (RC) delay time constant to monitor capacitance shift due to particle deposition in real-time and it is separately designed for re-use. The sensor chip is mounted on a custom-designed personal sampler and located away from center to increase the probability of accepting sub-micron particles while rejecting larger particles. The sensor showed a clear response with respect to particle deposition; and the positive capacitance shift is consistent with the increased sensor counting. Among the collected particles on the sensor, about 77 % are sub-micron particles whose diameter is below 1 μm, and most of the microscale particles appeared to be agglomerates of sub-micron particles. A comparison with simulation study shows that the sensor response using road dust is linearly proportional to the volume of particles. The concentration of collected particles on sensor is compared with a standard gravimetric method. Due to the radial dependence of particle deposition as well as sensor location, less than 1/1000 of the total particle mass is responsible for sensor response. With this calibration, the sensor response is represented as standard airborne particle concentration expression to demonstrate the sensor as a continuous particle monitoring device. Finally, the added microheater allows the sensor temperature to be maintained at constant temperature above dew point for stable sensor reading.

II. Device Fabrication

A. Sensor Design & Fabrication

The capacitive sensor was designed to be directly integrated with standard air sampling cassettes which use 25 - 37.5 mm filters. To demonstrate the capacitive sensor response, a custom-designed sampling cassette (Tsai Diffusion Sampler, TDS) is used [38]. The sampling cassette allows the selection of sub-micron particles while rejecting larger particles: the mass median aerodynamic diameter (MMAD) is 3.8 μm. The layout of sensor was determined such that it minimizes the air flow interference when integrated with the sampling cassette and facilitates easy connection with the readout board. Thus, the sensor strip has a rectangular shape with dimensions of 2 mm $\times$ 12 mm. The interdigitated patterns provide maximum sensitivity in a given area. As shown in Figure 1(a), the width of metal electrodes is 2 μm and two different versions of electrodes spacings are designed which are nominally either 2 μm or 3 μm. The electrodes spacings are chosen based on projected fabrication yield. The sensor is located at one end of the strip, and the actual sensing area is 1 mm $\times$ 1.5 mm.

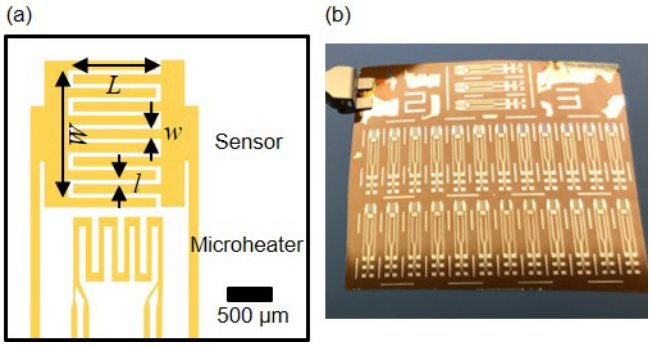

Fig. 1. (a) Interdigitated capacitive sensor strip layout. W = 1.5 mm, L = 1mm, w = 2 μm, and l = 2-3 μm. (b) Photograph of polyimide substrate containing sensor strips.

According to the Igreja and Dias, the capacitance of interdigitated patterns can be calculated as sum of interior capacitances (C_I) and exterior capacitances (C_E) with multiplication of the number of electrodes where C_I and C_E are capacitances with respect to a ground plane in the halfway between two electrodes [39]. Although the thickness of electrodes can be ignored when it is much thinner than the width of electrodes, in this work the ratio of thickness to width is only 1:5 (0.4 um: 2 um). For an accurate evaluation, a two-dimensional COMSOL simulation was performed with two electrodes on polyimide substrate as a unit. The 400 nm-thick electrodes are spaced by either 2 μm or 3 μm, the out-of-plane thickness representing the length of electrode is set as 1 mm. In order to understand both the capacitance of the interdigitated structure (without particles) and the effects of particle loading, COMSOL simulations were performed with different electrode thickness and spacing and the deposited particle layer is represented by a uniform-thickness layer of dielectric. The result is then normalized with respect to the entire sensor area.

Figure 2(a) shows the sensor response with different spacings. When there is no particle layer, the calculated capacitance is 8.37 pF for 2 μm spacing and 7.23 pF for 3 μm respectively. The capacitance increases linearly with increased particle layer thickness and begins to saturate as the layer thickness exceeds 400 nm. The slope in the linear region represents the sensitivity and it increases as the spacing is reduced. The results indicate that ΔC due to dielectric material is higher when particles are deposited in between electrodes. On the other hand,

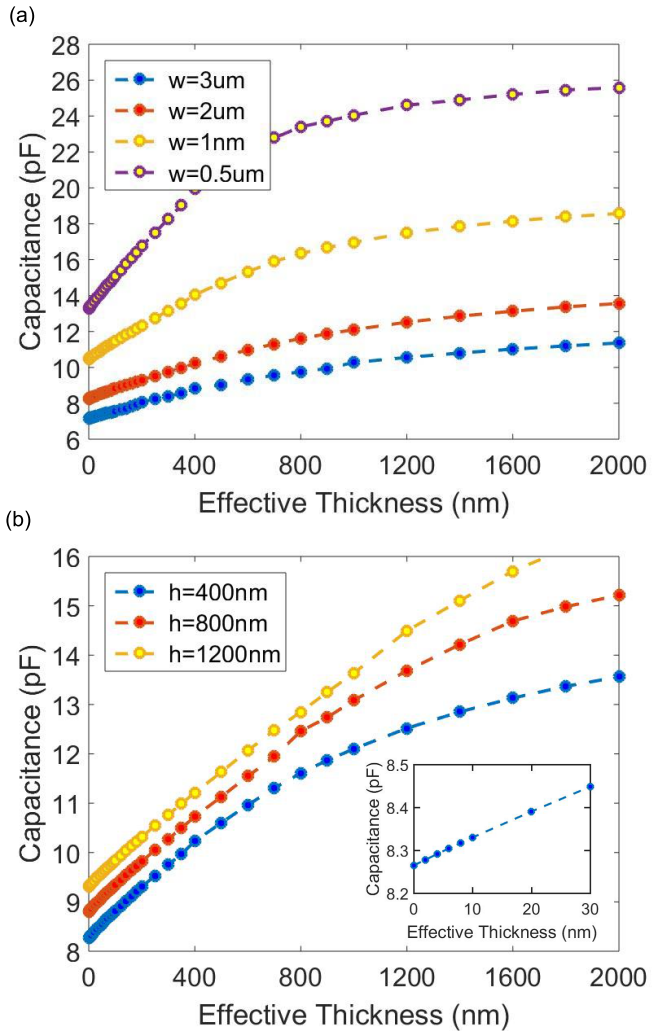

Fig. 2. A simulation result of capacitance response with (a) different electrodes width and (b) height. A uniform layer of particle is assumed with constant dielectric constant. The inset shows the capacitance response up to 30 nm at h = 400 nm and it is linearly proportional to the effective thickness.

Figure 2(b) shows the sensor response with different electrode heights. While the sensitivity remains constant, the saturation point is extended with increased electrodes height. Therefore, there is a trade-off between sensor spacing and sensitivity; a sensor with narrower spacing will be ideal for smaller particle detection but such a design will be inefficient for particles larger than the spacing as they will not be collected in between electrodes. Also, taller electrodes will be beneficial for extending the maximum capacity of sensor with constant response, but inefficient particle collection could happen as it could disturb airflow inside the sampler which disturb particle collection in between sensor.

The sensor strip also includes a resistance-based microheater suitable for maintaining the sensor at an elevated temperature; this capability provides a means to mitigate the effects of condensation/water droplets and enhances the stability of the capacitance. In addition, direct integration of microheater on sensor reduces the complexity of installing a heater inside the sampler, avoiding extra interfaces for heaters. The serpentine pattern is used in order to maximize the resistance (minimize the current) in the limited area, and four electrodes enable accurate temperature measurement as well. While silicon substrate provides solid and high fabrication yields, its high parasitic capacitance reduces the effect of capacitance change from the sensor. Polyimide has lower relative dielectric constant ($\varepsilon_{polyimide}$: 3.4) than silicon (ε_{Si}: 11.68) such that it minimizes the parasitic capacitance from the substrate. The flexible sensor/heater strips were batch-fabricated through scalable microfabrication approaches. A 127 um-thick polyimide film (Kapton HN, CS Hyde Company) was first degassed under vacuum oven for 8 hours to remove any remaining bubbles from the film. The film was then cut into square pieces and solvent-cleaned in the cleanroom facility. MCC Primer adhesion promotor (80/20, Microchem) and AZ 1518 positive photoresist were applied onto the polyimide substrate using a spin coater (Specialty Coating Systems G3). The photoresist layer was exposed using a mask aligner (Karl Suss MJB-3) and developed in MF-26A developer (Dow Electronic Materials MEGAPOST). Once the patterns were defined by photolithography, 20 nm of Titanium (Ti) and 400 nm of Aluminum (Al) were deposited via electron beam evaporation (Airco Temescal, System Control Technologies). This was done at a pressure level of 2.0×10^{-6} torr and a deposition rate of 1.0 – 2.0 Å/s. A lift-off process was performed by stripping off the photoresist using acetone. Figure 1(b) shows the sensors fabricated on polyimide substrate.

B. Interface PCB

To facilitate integration with the sampling cassette as well as the readout board, a custom-designed interface printed circuit board (PCB) is made. The interface PCB enables robust electrical and mechanical connections to the readout board, via the pin header connections. Figure 3(a) shows the interface PCB with sensor strip mounted. The sensor and microheater are wirebonded to the PCB using gold wires. Like batch-fabricated sensor strips, low-cost interface PCBs can be disposed with sensors as needed.

C. Integration With Sampling Cassette

The top portion of the sampling cassette was also modified from the original design so that the sensor could be inserted into the cassette. A detailed description of the original sampling cassette design was previously published [38]. The modification includes a 10 mm-long stand to support the sensor chip and an opening of 2.5 mm-height and 10 mm-width. To measure particle concentration after test, a polycarbonate filter covering the entire cross-section of air flow is placed on the bottom portion. The sensor is then inserted through the opening and located on the filter surface. The sensor is located approximately 2.5 mm away from the center as shown in Figure 3(b). After the sensor placement, the opening was sealed using paraffin wax film to avoid air leakage. About 15 % of the volume of sensor chip is inside the sampler. The assembled sensor (Figure 3(c)) is finally installed into the readout board as shown in Figure 3(d). The whole system has a dimension of 12 cm × 3 cm × 4 cm with total weight of 37 g.

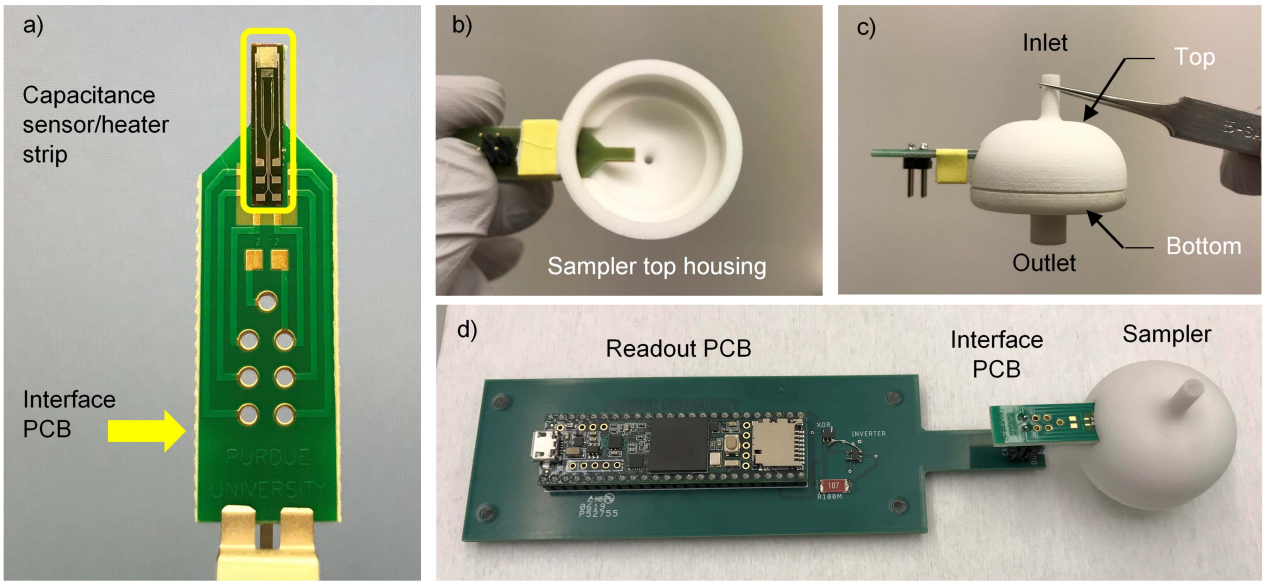

Fig. 3. Photographs of a) capacitance sensor/heater strip mounted on interface PCB; b) and c) strip/interface PCB assembly mounted in a modified sampling cassette, showing bottom view of top housing and side view of full sampler, respectively; and d) fully assembled system. The sensor/cassette assembly is electrically connected to the separately designed readout board. The readout board can be re-used.

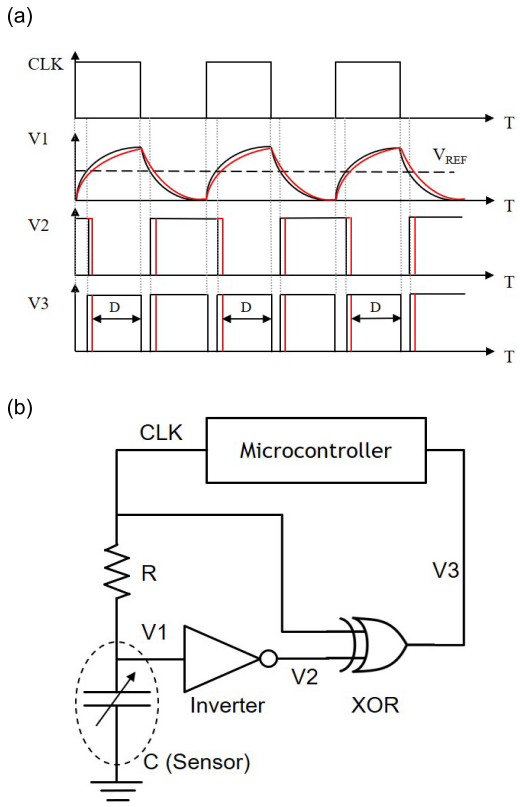

Fig. 4. a) Ideal response of sensor readout. The time constant delay as a result of capacitance shift (red curve) is reflected on the duration of output pulses (V3). b) Block diagram of capacitive sensor and readout configuration.

D. Readout Circuit

Figure 4 shows an ideal response of the readout circuit and the block diagram of the sensor and readout circuit. The integrated readout approach measures the time constant of an electrical circuit consisting of the capacitance sensor and an external resistor (100 MΩ ± 5%, Bourns Inc.) [40]. The operation procedure is as follows: i) The microcontroller (Teensy 3.6, PJRC) generates a clock signal (CLK) of 100 Hz (square wave, 50 % duty cycle), ii) the resistance-capacitance delay (RC delay) influences the clock signal depending on the RC time constant (V1), iii) The wave form is then transformed into a square wave signal (V2) after passing the inverter (SN74AUP1G04DBVT, Texas Instrument), iv) the output of the inverter is fed into the XOR gate (74HC1G86GV, Nexperia USA Inc.) and compared with the initial clock signal, v) the final XOR output (V3) is then sent back to the microcontroller. The duration of output pulses (D) are counted by the microcontroller. Counting interval (minimum detectable pulse width) is set to 1 microseconds (μS) and the switching threshold of the inverter (V_{REF}) is set to 0.5 V_{DD}. The "rise" pulse in V3 appeared to be more sensitive than the "fall" pulse where it could be related to the value of V_{REF}. Therefore, only the "rise" pulses are chosen for counting and the counting results of 500 pulses are averaged. As the capacitance of the sensor increases due to particle deposition, the corresponding increase in the time constant of the RC circuit (red curve) is converted into a shift in counts in a sampling circuit, realized by the microcontroller. The data from the microcontroller can be downloaded through a USB port.

III. Results & Discussions

A. Calibration & Test Set Up

The fabricated sensor chips are measured using tabletop impedance analyzer (Keysight, E4990A). The capacitance of sensor chips includes the sensor strip and interface PCB. For the 2 μm-spacing sensor chips, the measured capacitances ranged from 11 to 12 pF and the 3 μm-spacing sensor chips have capacitance of 7 - 8 pF. Comparing with the calculated nominal capacitances of 2 μm and 3 μm-spacing sensors,

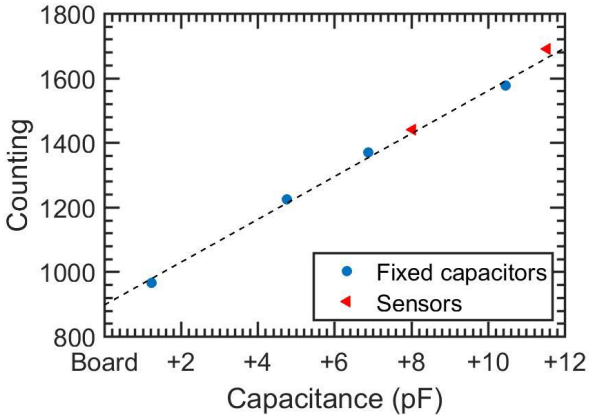

Fig. 5. Readout circuit calibration using fixed capacitors. Fixed capacitance values (blue) are 1.24 pF, 4.76 pF, 6.88 pF, and 10.47 pF respectively. The tested sensor chips (red) fit to the linearly extrapolated curve (black).

which are 8.37 pF and 7.23 pF respectively, the higher measured values should originate from the parasitic capacitance of the interface PCB as well as fabrication nonidealities. The measured capacitance values with a tabletop capacitance meter has an accuracy of ±0.02 picofarad (pF) and the counting accuracy is ±0.5. The sensor sensitivity is estimated by calculating the RC time constant (τ) as a result of capacitance shift. That is,

$$V = V_0(1 - e^{-\frac{t}{\tau}}). \quad (1)$$

where V_0 is an initial voltage and t represents time. Using MATLAB simulation, it appears that about 15 femtofarad (fF) of capacitance shift is required to delay 1 μs of rising time reaching the V_{REF}. Four different capacitors with known values are used for linear extrapolation, as shown in Figure 5. The inverse of slope is 15.1 fF/count which matches with our estimation. Because the readout board itself has a fixed resistance and parasitic capacitance, a non-zero number of counts is observed for zero sample capacitance. The results showed that counting increased linearly with increasing capacitance. After calibration with the fixed capacitors, the actual capacitive sensor chips were compared. The counting of two sensor chips (8.03 pF and 11.54 pF) matched well with the linearly extrapolated curve.

B. Test With Road Dust

The capacitance sensing approach was demonstrated with test dust, with the capacitance sensor mounted in the sampler. A custom-designed test chamber (20 cm × 20 cm × 20 cm) is prepared and two openings are made on the side wall and the top side respectively. The assembled modified sampler was mounted on the outside of wall, and the inlet of the sampler was inserted through the opening in the side wall. The outlet of the sampler was connected to an air pump for constant air flow (0.3 L/min), and road dust (Arizona Test Dust, ISO12103-1, Powder Technology Inc.) was sprayed periodically through the top opening of the chamber. Since the dust consists primarily of silica, it was assumed that the dielectric constant of the test dust is same as that of silica, which is 3.9. The readout PCB

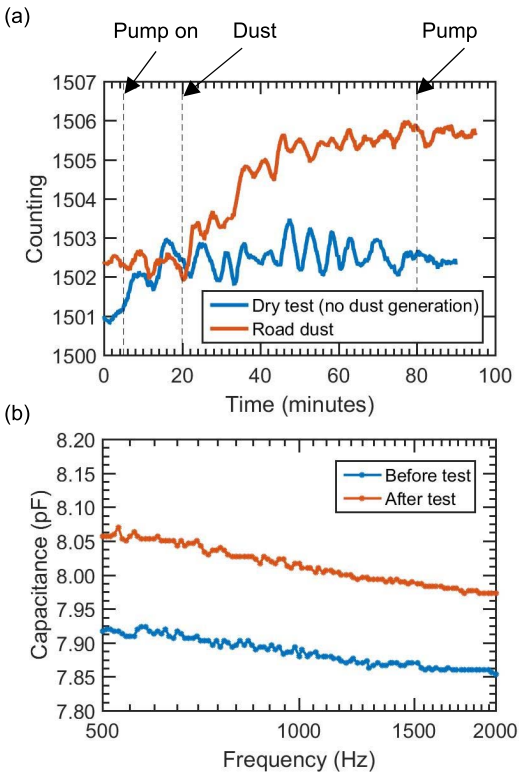

Fig. 6. a) Time-response of an integrated sampler, comparing i) test with road dust and ii) a "dry" test, without particle generation. A clear differential response was observed for the case in which particles were generated in the chamber volume. b) Capacitance shift before/after testing, as measured by a laboratory capacitance meter. The positive shift in capacitance is consistent with increased counting.

was connected to a computer via a USB port for real-time sensor monitoring.

Figure 6(a) shows the time-response of a sensor device during two tests: one using road-dust and the other with the same airflow but without particles. At the beginning of each test, the stability of the sensor was monitored via measurement during 5 minutes without airflow and 15 minutes of airflow without particles. After 60 minutes of tests, an additional 10 minutes of measurement without air flow was performed. While the sensor reading was stable during dry test (no particles generated), a clear differential response was observed when particles are generated showing a counting shift of 3.24 counts. This indicates that the duration of output pulse changed by 3.24 μs as a result of capacitance change. The sub-integers of counts are the results of averaging as described in the readout circuit section as well as 2 minutes of window averaging from the recorded data. The sensor capacitance was measured before/after test for comparison and Figure 6(b) shows an increase in sensor capacitance after testing, in agreement with positive shifts in counting from the readout circuit. The frequency dependence of capacitance is observed from the sensor chip before and after test; the frequency-dependent dielectric constant of polyimide substrate could reduce the capacitance with increased frequency [41]. The readout calibration using fixed capacitors estimated a resolution of ~15 fF/count, however, the calculated resolution from the test results using road dust appeared to be ~42 fF/count.

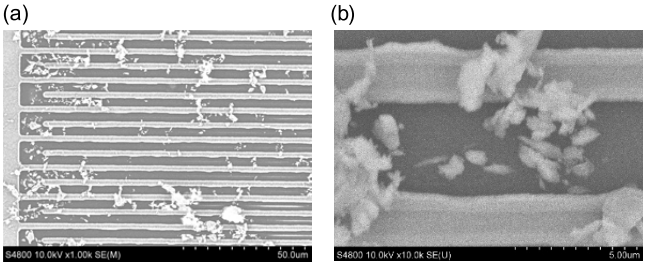

Fig. 7. SEM image of a) particles deposited on a capacitance sensor after exposure to comparable particle flux. For reference, the lines and spaces in the image are approximately 3 microns. b) A magnified SEM image showing agglomerates of sub-micron particles.

TABLE I
POST-ANALYSIS OF PARTICLE INFORMATION USING SEM

Group	Size range	D_{eff} (μm)	# of Particles	V_{eff} (μm^3)	m_{eff} (g)	Fraction (%)
A	D ≤ 1 μm	0.5	10,005	6.5×10^{2}	1.7×10^{-9}	5.7
B	1 < D ≤ 2 μm	1.5	2,728	4.8×10^{3}	1.3×10^{-8}	42.1
C	2 < D ≤ 3 μm	3	140	2.0×10^{3}	5.3×10^{-9}	17.3
D	3 < D ≤ 4 μm	4	120	4.0×10^{3}	1.1×10^{-8}	34.9
Total			12,993	1.2×10^{4}	3.0×10^{-8}	100

One possibility is that the actual capacitance shifts due to particles could be masked under continuous air flow which causes dried condition, resulting the reduced capacitance shifts during tests.

C. Correlation of Sensor Response to Total Particles Estimated From Post-Test Imaging

The tested sensor was inspected with a scanning-electron microscope (SEM) for post-analysis. Five SEM images with a fixed magnification are inspected, and the average number of particles are calibrated with respect to the entire size of sensor. Figure 7(a) shows one of the SEM images of a capacitance sensor exposed to a comparable flux of particles. The collected particles are binned by size based on SEM images, as listed in Table I. About 77 % of particles are smaller than 1 μm while 23 % are larger than 1μm. Whereas most particles had sub-micrometer diameters, a few larger particles were observed; each of these is counted as a single particle due to a limited resolution. In order to estimate total volume of particles within each size range, particles are assumed as spheres with an average diameter (D_{eff}) corresponding to each bin. By summing the estimated volumes for all size ranges, the total volume of particles on the sensor is calculated to be 1.15×10^4 μm^3. Since the test dust mostly consists of silica, the density of silica (2.65 g/cm^3) is used for the calculation of the effective mass (m_{eff}). The calculated total m_{eff} on sensor is 3×10^{-8} g. The calculation indicates that the positive capacitive sensor response corresponds to the volume of particles collected on sensor. As summarized in Table I, although a large fraction of the overall particle count comes from sub-micron particles, the total volume of particulate material is dominated by the particles larger than 1 micron. The volume fraction of each particle size range should correlate to the relative contribution to capacitance response. It should be noted that a magnified SEM image shows that those larger particles were the agglomerates of sub-micron particles rather than single particles as shown in Figure 7(b). Nucleation of particles after landing on sensor could result such agglomerations, but a comparative study with aerosol size distribution of test dust, collection time, and particle concentration are necessary to understand the agglomerations.

To understand the sensor sensitivity with volume, the calculated volume is compared with simulation results in Figure (2). The total volume is converted into effective thickness (T_{eff}), i.e. the thickness of a uniform thin film containing the same volume of material. Assuming the material is uniformly deposited over the sensing area (1 mm × 1.5 mm), the T_{eff} is estimated to be ∼8 nm. This T_{eff} is then compared with a simulation result. The inset in Figure 2(a) shows that sensor sensitivity is constant with thickness. Since the effective thickness is about 8 nm, sensor response is in the regime where the dielectric change is linearly proportional to the volume of each particle. While the fractional change in capacitance ($\Delta C/C$) from experiment is about 1.7 %, that from simulation becomes 0.6 % with 8 nm of increase in T_{eff}. Although it requires 20 nm to reach the equivalent $\Delta C/C$ from experiment, the comparison using $\Delta C/C$ still shows that our sensor response is in the linear regime.

D. Effective Particle Concentration

The collected mass on the sensor are compared with a standard gravimetric method. The 25 mm polycarbonate filters were desiccated for a minimum of 48 hours prior to pre and post weighing. Filters were weighed on a microbalance (Mettler Toledo MX5) until two consecutive measurements were within 0.005 mg. The two measurements were averaged to determine the final weight, which is 4×10^{-5} g. Comparing with the collected mass on sensor as shown in Table I, the average mass on filter (sampler) is more than three orders of magnitude higher than that on sensor. Considering that the sensing area is about 0.33% of the filter area (13% including interface PCB), the larger mass ratio than the area ratio indicates a size-dependent distribution of particles inside the sampler. Figure 8(a) shows a clear image wherein a high portion of larger particles was collected at the center area, and the deposition of larger particles decreased with distance from the center. This is mainly due to the inertia force of micrometer sized particles where it faces airflow directly. It also shows that the sensor and interface board attached on the filter do not interfere with particle deposition on the filter, grid, and sensor respectively. The relatively clean area at the lower side of the filter indicates the sensor and interface board location.

A simulation study using a computational fluid dynamic program showed that particle distribution inside the sampling cassette depends on the particle size; particles smaller than 3 μm are uniformly distributed over the filter area, while particles larger than 3 μm are concentrated in the center area. Figure 8(b) shows the simulation results with three representative particles; while particles of 11.5 nm-diameter (red)

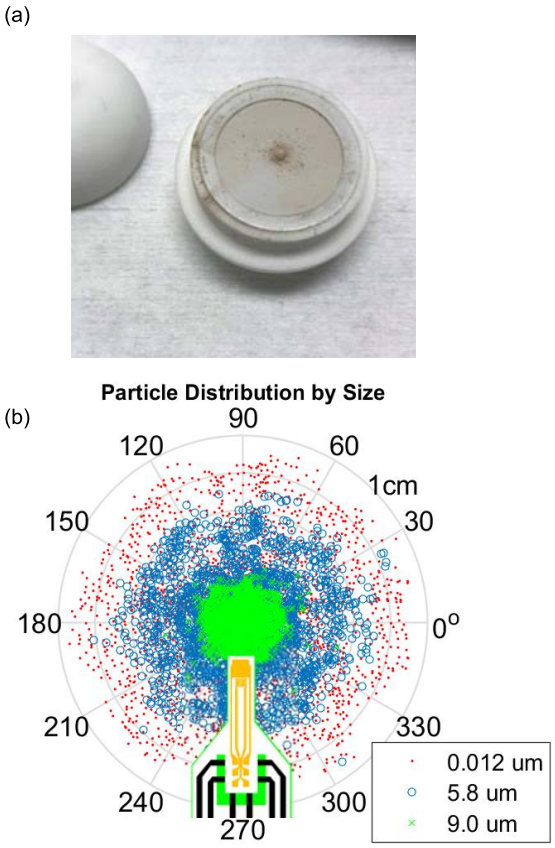

Fig. 8. (a) Photograph of the filter after testing. A high proportion of particles was collected at the center area, and the concentration decreased with increasing radius. (b) Radial distribution of particle by size. Small dots (red) represent particles with 12 nm diameter, circles (blue) represent particles with 5.8 μm, and crosses (green) represent particles with 9.0 μm. The radius of each circle represents 0.2, 0.4, 0.6, 0.8, and 1 cm, respectively.

is uniformly distributed, both 5.8 um-diameter (blue) and 9.0 um-diameter (green) are collected preferably in the center. The sensor is located about 2.5 mm away from the center. According to the simulation result, the sensor rejects most of particles larger than 9 μm while some of 5 μm-diameter particles could land on the sensor. This result agrees with our post-analysis on Table I where a small portion of microparticles are observed on the sensor. Therefore, placing the sensor away from the center increases the probability of accepting sub-micron particles rather than microparticles.

With all given information, we can convert our results into the standard particle concentration expression; g/m^3. Using the chain rule,

$$\frac{mass\,(g)}{Volume\,(m^3)} = \frac{Count}{min} \times \left(\frac{mass\,(g)}{Count} \times \frac{1}{Flowrate(L/min)} \times C\right) \quad (2)$$

where C is the mass calibration factor. The C represents the ratio of particle mass on filter to particle mass on sensor, which are obtained by gravimetric method and post-analysis respectively. While the terms in the parenthesis are known, only the rate of change in count will vary with respect to the environment. For instance, the rate of change in Figure 6(a) is about 1 count/10 minutes for the first 30 minutes. Therefore,

$$4.11\frac{mg}{m^3} = \frac{1Count}{10min} \times \left(\frac{3.04 \times 10^{-8}\,(g)}{3.24Count} \times \frac{1}{0.3(L/min)} \times \frac{10^3 L}{m^3} \times 1,316\right). \quad (3)$$

The calculation result shows that under the given test conditions using road dust, the particle concentration is ~4 mg/m^3 for 10 minutes of sampling. On the other hand, the rate decreases after 30 minutes of particle sampling with the ratio of 0.33 count/10 minutes. That is,

$$1.36\frac{mg}{m^3} = \frac{0.33Count}{10min} \times \left(\frac{3.04 \times 10^{-8}\,(g)}{3.24Count} \times \frac{1}{0.3(L/min)} \times \frac{10^3 L}{m^3} \times 1,316\right). \quad (4)$$

By monitoring the rate of change in counts, the airborne particle concentration can be calculated at intervals on the order of 10-20 minutes.

E. Microheater Characterization

The microheater integrated on the sensor strip allows heating of the strip to a controlled elevated temperature. This is intended to mitigate effects of high and variable ambient humidity as well as temperature-based drift in capacitance under constant air flow. Figure 9(a) shows the capacitance reading without and with the heater activated in ambient condition (Temperature: 19 °C, Relative humidity: 38%). Under constant air flow (no particles generated), the use of heater resulted in a more stable sensor capacitance where the variation reduced from ±40 fF to ±20 fF, thus enabling stable detection of a smaller quantity of deposited particles. The absolute capacitance decreased after heater is activated.

Figure 9(b) shows the IR microscope image of sensor when heater is activated. When 22mW of power was applied to heater, the average sensor temperature increased by 10-15 °C compared to room temperature. As a result, the amount of adsorbed water on the sensor should decrease, resulting a decreased capacitance. The effect of thermal expansion is negligible since the estimated lateral thermal expansion of 2 mm-wide polyimide film is tens of nanometers (Coefficient of thermal expansion of polyimide film: 20×10^{-6}°C^{-1}).

Figure 10 shows the stability of the capacitance signal as a function of RH at room temperature. To control the RH, air was bubbled through a beaker of water inside the test chamber and the RH was measured using hygrometer. No sampling cassette is used to eliminate the effect of air flow. While capacitance increased with higher RH, the use of the on-board resistance heater significantly decreased the variation in capacitance over the range of 43–64 % RH (dew point of 5.6 °C to 12 °C). Like Figure 9, the absolute capacitance decreased again as heater is activated but remained stable during operation. This result indicates that the capacitance sensor can operate over a range of ambient dew points.

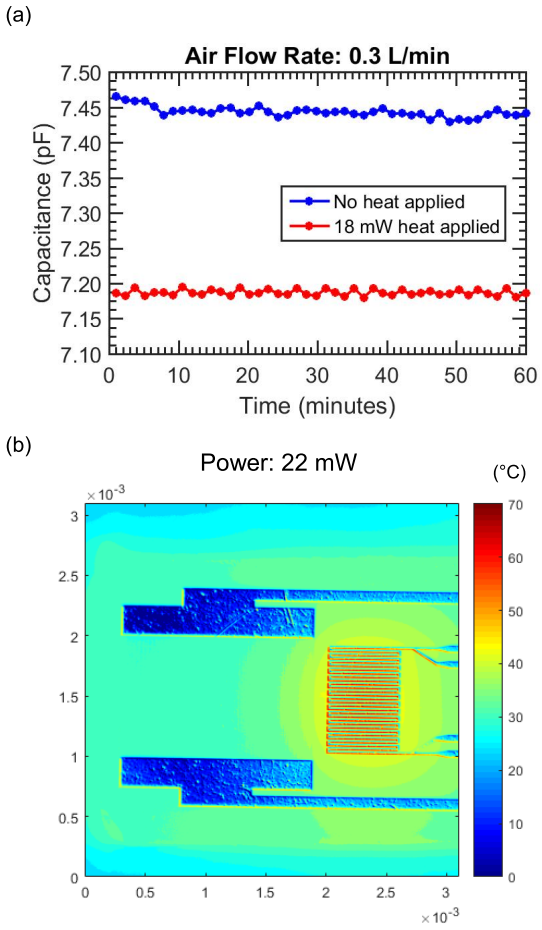

Fig. 9. (a) Capacitance sensor test without and with heating via a resistance heater. Tests were performed at constant flow rate and capacitance fluctuation is reduced with the activation of heater. (b) IR microscope image of sensor/heater strip. Sensor temperature increased by 10-15 °C with heater activation.

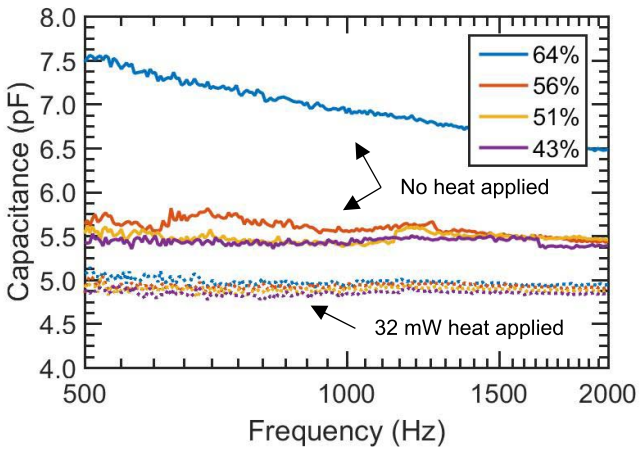

Fig. 10. Capacitance response at different relative humidity levels without a heater and with an activated heater. The stability of capacitance improved specifically at higher relative humidity (or dew point) when heater is activated.

IV. Conclusion

An interdigitated capacitive sensor is made for sub-micron and nanoscale particulate matters detection in the mining environment. The batch-fabricated sensor strip is designed for the integration with personal sampling cassettes and the readout board enables continuous monitoring of capacitance shifts due to particles. Sensor response with respect to test dust showed differential behavior from tests without dust and good agreement with positive capacitance shift. Most of the collected particles appeared to be sub-micrometer sized particles with diameter below 1 μm, and micrometer sized particles are agglomerates of smaller particles. A simulation study showed that our sensor response is linearly proportional to the volume of collected particles. The particle mass on sensor with the consideration of radial dependence of particle deposition and sensor location can estimate the total mass concentration of deposited particles. The incorporated heater improved stable capacitance sensor reading by mitigating variations from surroundings such as air flow and relative humidity. Finally, the sensor response is converted into a standard airborne particle concentration (g/m^3) demonstrating an example of continuous particle monitoring. This disposable and real-time particle sensing device could be integrated with standard personal sampling cassettes and utilized for workers in the mining environmental and other diverse workplaces who are exposed to hazardous sub-micrometer and nanometer-sized particles.

Acknowledgment

The authors would like to thank Nathan Krumland for assisting the simulation of particle deposition on the sampling filter. The views, opinions and recommendations expressed herein are solely those of the authors and do not imply any endorsement by the Alpha Foundation, its Directors and staff. In addition, its contents are solely the responsibility of the authors and do not necessarily represent the official views of the Centers for Disease Control and Prevention or the Department of Health and Human Services.

References

[1] D. Glover and K. Cram, "Respirable airborne dust exposure levels in the New South Wales coal mining industry," *Appl. Occupational Environ. Hygiene*, vol. 12, no. 12, pp. 980–987, Dec. 1997.

[2] *Coal Mine Dust Exposures and Associated Health Outcomes; A Review of Information Published Since 1995*, Niosh, Cincinnati, OH, USA, 2011.

[3] "Lowering miners' exposure to respirable coal mine dust, including continuous personal dust monitors," Dept. Labor, Mine Saf. Health Admin., Arlington, VA, USA, Tech. Rep. 2014-09084, 2014, pp. 24813–24994.

[4] R. I. Higgins and P. Dewell, "A gravimetric size-selecting personal dust sampler," in *Inhaled particles and vapours*. Oxford, U.K.: Pergamon Press, 1967, pp. 575–586.

[5] S. Gaillard, E. Sarver, and E. Cauda, "A field study on the possible attachment of DPM and respirable dust in mining environments," *J. Sustain. Mining*, vol. 18, no. 2, pp. 100–108, May 2019.

[6] R. Ferrante, F. Boccuni, F. Tombolini, and S. Iavicoli, "Measurement techniques of exposure to nanomaterials in workplaces," in *Nanotechnology in Eco-Efficient Construction*. Cambridge, U.K.: Woodhead Publishing, Jan. 2019, pp. 785–813.

[7] C. C. Gravati, "Real time measurement of the size distribution of particulate matter by a light scattering method," *J. Air Pollut. Control Assoc.*, vol. 23, no. 12, pp. 1035–1038, Dec. 1973.

[8] J. W. Sadowski and E. Byckling, "Apparatus for real-time measurement of particle size distribution," *Powder Technol.*, vol. 20, no. 2, pp. 273–284, Jul. 1978.

[9] G. J. Chekan, J. F. Colinet, F. N. Kissell, J. P. Rider, R. P. Vinson, and J. C. Volkwein, "Performance of a light-scattering dust monitor in underground mines," *Trans. Soc. Mining, Metall. Explor. Inc.*, no. 320, pp. 21–24, 2007.

[10] J. C. F. Wang, H. Patashnick, and G. Rupprecht, "A new real-time isokinetic dust mass monitoring system," *J. Air Pollut. Control Assoc.*, vol. 30, no. 9, pp. 1018–1021, Sep. 1980.

[11] U.S. National Institute for Occupational Safety and Health. (2016). *CPDM Helps Coal Miners Avoid Hazardous Dust Center for Disease Contronl and Prevention*. [Online]. Available: https://www.cdc.gov/niosh/mining/features/CPDMhelpsminersavoiddust.html

[12] T. K. Ervik, N. Benker, S. Weinbruch, Y. Thomassen, D. G. Ellingsen, and B. Berlinger, "Size distribution and single particle characterization of airborne particulate matter collected in a silicon carbide plant," *Environ. Sci., Processes Impacts*, vol. 21, no. 3, pp. 564–574, Mar. 2019.

[13] A. S. Fonseca *et al.*, "Particle release and control of worker exposure during laboratory-scale synthesis, handling and simulated spills of manufactured nanomaterials in fume hoods," *J. Nanoparticle Res.*, vol. 20, no. 2, p. 48, Feb. 2018.

[14] J. Heyder, J. Gebhart, G. Rudolf, C. F. Schiller, and W. Stahlhofen, "Deposition of particles in the human respiratory tract in the size range 0.005–15 μm," *J. Aerosol Sci.*, vol. 17, no. 5, pp. 811–825, Jan. 1986.

[15] T. Li *et al.*, "Fine particulate matter (PM2.5): The culprit for chronic lung diseases in China," *Chronic Diseases Translational Med.*, vol. 4, no. 3, pp. 176–186, Sep. 2018.

[16] M. J. Ellenbecker and C. S. J. Tsai, *Exposure Assessment and Safety Considerations for Working With Engineered Nanoparticles*. Hoboken, NJ, USA: Wiley, 2015.

[17] P. A. Schulte *et al.*, "Focused actions to protect carbon nanotube workers," *Amer. J. Ind. Med.*, vol. 55, no. 5, pp. 395–411, May 2012.

[18] S.-H. Liou, C. S. J. Tsai, D. Pelclova, M. K. Schubauer-Berigan, and P. A. Schulte, "Assessing the first wave of epidemiological studies of nanomaterial workers," *J. Nanoparticle Res.*, vol. 17, no. 10, pp. 1–19, Oct. 2015.

[19] M. Ellenbecker *et al.*, "The difficulties in establishing an occupational exposure limit for carbon nanotubes," *J. Nanoparticle Res.*, vol. 20, no. 5, p. 131, May 2018.

[20] *Nanomaterial Production and Downstream Handling Processes*, NIOSH, OH, USA, 2013.

[21] M. W. Tessum and P. C. Raynor, "Effects of spray surfactant and particle charge on respirable coal dust capture," *Saf. Health at Work*, vol. 8, no. 3, pp. 296–305, Sep. 2017.

[22] H. S. Wasisto, S. Merzsch, A. Waag, E. Uhde, T. Salthammer, and E. Peiner, "Airborne engineered nanoparticle mass sensor based on a silicon resonant cantilever," *Sens. Actuators B, Chem.*, vol. 180, pp. 77–89, Apr. 2013.

[23] U. Soysal, F. Marty, E. Algre, E. Gehin, and C. Motzkus, "Sub-μm air-gap resonant MEMS mass sensors fabrication and electrical characterization for the detection of airborne particles," in *Proc. Symp. Design, Test, Integr. Packag. MEMS MOEMS (DTIP)*, May 2018, pp. 1–5.

[24] I. Paprotny, F. Doering, P. A. Solomon, R. M. White, and L. A. Gundel, "Microfabricated air-microfluidic sensor for personal monitoring of airborne particulate matter: Design, fabrication, and experimental results," *Sens. Actuators A, Phys.*, vol. 201, pp. 506–516, Oct. 2013.

[25] A. Hajjam, J. C. Wilson, and S. Pourkamali, "Individual air-borne particle mass measurement using high-frequency micromechanical resonators," *IEEE Sensors J.*, vol. 11, no. 11, pp. 2883–2890, Nov. 2011.

[26] S. V. Hering, M. R. Stolzenburg, F. R. Quant, D. R. Oberreit, and P. B. Keady, "A laminar-flow, water-based condensation particle counter (WCPC)," *Aerosol Sci. Technol.*, vol. 39, no. 7, pp. 659–672, Jul. 2005.

[27] T. Lu *et al.*, "High sensitivity nanoparticle detection using optical microcavities," *Proc. Nat. Acad. Sci. USA*, vol. 108, no. 15, pp. 9–5976, Apr. 2011.

[28] X. C. Yu, Y. Zhi, S. J. Tang, Q. Gong, C. W. Qiu, and Y. F. Xiao, "Optically sizing single atmospheric particulates with a 10-nm resolution using a strong evanescent field," *Light Sci. Appl.*, vol. 7, no. 4, p. 18003, Apr. 2018.

[29] R. Xu, "Light scattering: A review of particle characterization applications," *Particuology*, vol. 18, pp. 11–21, Feb. 2015.

[30] O. Hogrefe, G. G. Lala, B. P. Frank, J. J. Schwab, and K. L. Demerjian, "Field evaluation of a TSI model 3034 scanning mobility particle sizer in new york city: Winter 2004 intensive campaign," *Aerosol Sci. Technol.*, vol. 40, no. 10, pp. 753–762, Oct. 2006.

[31] M. Bertke, W. Wu, H. S. Wasisto, E. Uhde, and E. Peiner, "Size-selective electrostatic sampling and removal of nanoparticles on silicon cantilever sensors for air-quality monitoring," in *Proc. 19th Int. Conf. Solid-State Sensors, Actuat. Microsyst. (TRANSDUCERS)*, Jun. 2017, pp. 1493–1496.

[32] H. S. Wasisto, S. Merzsch, E. Uhde, A. Waag, and E. Peiner, "Handheld personal airborne nanoparticle detector based on microelectromechanical silicon resonant cantilever," *Microelectronic Eng.*, vol. 145, pp. 96–103, Sep. 2015.

[33] M. Fierz, D. Meier, P. Steigmeier, and H. Burtscher, "Miniature nanoparticle sensors for exposure measurement and TEM sampling," *J. Phys., Conf. Ser.*, vol. 617, May 2015, Art. no. 012034.

[34] L. Yuen, W. C. Chu, and B. Stoeber, "Microfluidic-based real-time detector for fine particulate matter," in *Proc. IEEE SENSORS*, Nov. 2014, pp. 775–778.

[35] I. Evans and T. York, "Microelectronic capacitance transducer for particle detection," *IEEE Sensors J.*, vol. 4, no. 3, pp. 364–372, Jun. 2004.

[36] P. Ciccarella, M. Carminati, M. Sampietro, and G. Ferrari, "Multichannel 65 ZF rms resolution CMOS monolithic capacitive sensor for counting single micrometer-sized airborne particles on chip," *IEEE J. Solid-State Circuits*, vol. 51, no. 11, pp. 2545–2553, Nov. 2016.

[37] M. Carminati, G. Ferrari, and M. Sampietro, "Emerging miniaturized technologies for airborne particulate matter pervasive monitoring," *Measurement*, vol. 101, pp. 250–256, Apr. 2017.

[38] C. S.-J. Tsai and D. Theisen, "A sampler designed for nanoparticles and respirable particles with direct analysis feature," *J. Nanoparticle Res.*, vol. 20, no. 8, p. 209, Aug. 2018.

[39] R. Igreja and C. J. Dias, "Analytical evaluation of the interdigital electrodes capacitance for a multi-layered structure," *Sens. Actuators A, Phys.*, vol. 112, nos. 2–3, pp. 291–301, May 2004.

[40] J. H.-L. Lu, M. Inerowicz, S. Joo, J.-K. Kwon, and B. Jung, "A low-power, Wide-Dynamic-Range semi-digital universal sensor readout circuit using pulsewidth modulation," *IEEE Sensors J.*, vol. 11, no. 5, pp. 1134–1144, May 2011.

[41] S. Chisca, V. E. Musteata, I. Sava, and M. Bruma, "Dielectric behavior of some aromatic polyimide films," *Eur. Polym. J.*, vol. 47, no. 5, pp. 1186–1197, May 2011.